Supplement of Atmos. Chem. Phys., 22, 6291–6308, 2022
https://doi.org/10.5194/acp-22-6291-2022-supplement

Supplement of

Trends in secondary inorganic aerosol pollution in China and its responses to emission controls of precursors in wintertime

Fanlei Meng et al.

Correspondence to: Wen Xu (wenxu@cau.edu.cn) and Shaocai Yu (shaocaiyu@zju.edu.cn)

S1: Method1: Calculation of other parameters from meta-analysis

Sulfur oxidation ratio (SOR) and nitrogen oxidation ratio (NOR) are indicators of secondary pollutant transformation in the atmosphere (Sun et al., 2006; Xu et al., 2017). Higher SOR and NOR values imply greater oxidation of gaseous species to sulfate- and nitrate-containing secondary particles (Sun et al., 2006), respectively. Their formulae are as follows, where *n* refers to the molar concentrations:

$$SOR = nSO_4^{2-}/(nSO_4^{2-} + nSO_2) \tag{1}$$

$$NOR = nNO_3^{-}/(nNO_3^{-} + nNO_2) \tag{2}$$

To identify whether acidic species are fully neutralized by NH_3 in $PM_{2.5}$, we selected two indicators: the slope of the linear regression between equivalent concentrations of $[NH_4^+]$ and $[SO_4^{2-}]$ and the slope of the linear regression between equivalent concentrations of $[NH_4^+]$ and $[SO_4^{2-} + NO_3^-]$ (Sun et al., 2006). In the atmosphere, NH_3 is first taken up by sulfuric acid to form ammonium sulfate salts and then any excess NH_3 may then react with nitric and hydrochloric acids to form ammonium nitrate and ammonium chloride (Ianniello et al., 2010). When the slope of NS is less than 1, NH_3 is not completely neutralized with sulfuric acid and nitric acid, suggesting a NH_3-limited environment. Slopes of NS and NSN greater than 1 indicate that they reacted completely, suggesting a NH_3-rich environment (Xu et al., 2017).

S2: Method2: Additional information about the monitoring data

The concentrations of $PM_{2.5}$, SO_2, and NO_2 were measured at state-controlled air sampling sites located within each city or county. To avoid direct influence of potential air pollution sources, most of the monitoring sites were situated in background locations in the urban areas. Concentrations of $PM_{2.5}$ were measured using the micro oscillating balance method (TEOM from Rupprecht & Patashnick Co., Inc.,USA) or the β absorption method (BAM 1020 from Met One Instrument Inc., USA; Tianhong Co., China or Xianhe Co., China). Concentrations of SO_2 were measured using either UV-spectrophotometry (TEI Model 49i from Thermo Fisher Scientific Inc., USA) or Ultraviolet Fluorescence (TEI Model 43i from Thermo Fisher Scientific Inc., USA) methods, and concentrations of NO_2 using the chemiluminescence (TEI Model 42i from Thermo Fisher Scientific Inc., USA) method. The detection limits (DL) of these techniques are sufficient to measure accurately the high or relatively high concentration of $PM_{2.5}$, SO_2, and NO_2 at all monitoring sites.

Data from all monitoring sites were automatically released to an open website after validation using HJ630-2011 specifications (http://kjs.mep.gov.cn/hjbhbz/bzwb/other/qt/201109/W020120130585014685198.pdf). The instruments for $PM_{2.5}$ measurements were tested using the reference method by at least three samples based on HJ 618 specifications. The instruments used for SO_2 and NO_2 measurement at each site were tested for zero and scale noises, error of indication, zero and span drifts, etc.

Along with the acid gases, surface NH_3 concentrations over China for the 2008–2016 period (the current availability) was extracted from the study of Liu et al. (2019), which were estimated using IASI (the Infrared Atmospheric Sounding Interferometer) NH_3 retrievals and NH_3 vertical profiles (Fig. S9). Although the satellite-derived surface NH_3 concentrations are described in detail by Liu et al. (2019), a brief summary is given here for the reader's convenience. The NH_3 total columns were derived from the IASI-A instrument (aboard the MetOp-A platform) morning overpass observations (i.e., 09:30 local time at the Equator during overpass), which have a circular footprint of 12 km diameter at nadir and an ellipsoid shaped footprint of up to 20 km × 39 km at the maximum diameter (Van Damme et al., 2018). The IASI NH_3 datasets are the ANNI-NH_3-v2.2R-I retrieval product, which was developed by converting hyperspectral range index data to NH_3 columns using an Artificial Neural Network for IASI (ANNI) algorithm (Whitburn et al., 2016). The NH_3 vertical profiles were simulated from the Goddard Earth Observing System-Chemistry (GEOS-Chem) atmospheric transport model considering H_2SO_4-HNO_3-NH_3 aerosol thermodynamics mechanisms (Whitburn et al., 2016; Van Damme et al., 2017), and were used to convert the satellite NH_3 columns to surface NH_3 concentrations. The satellite NH_3 predictions are reliable (average $R^2 = 0.919$ and $p<0.001$) by validating against the in-situ surface observations on a monthly basis (Liu et al., 2019)

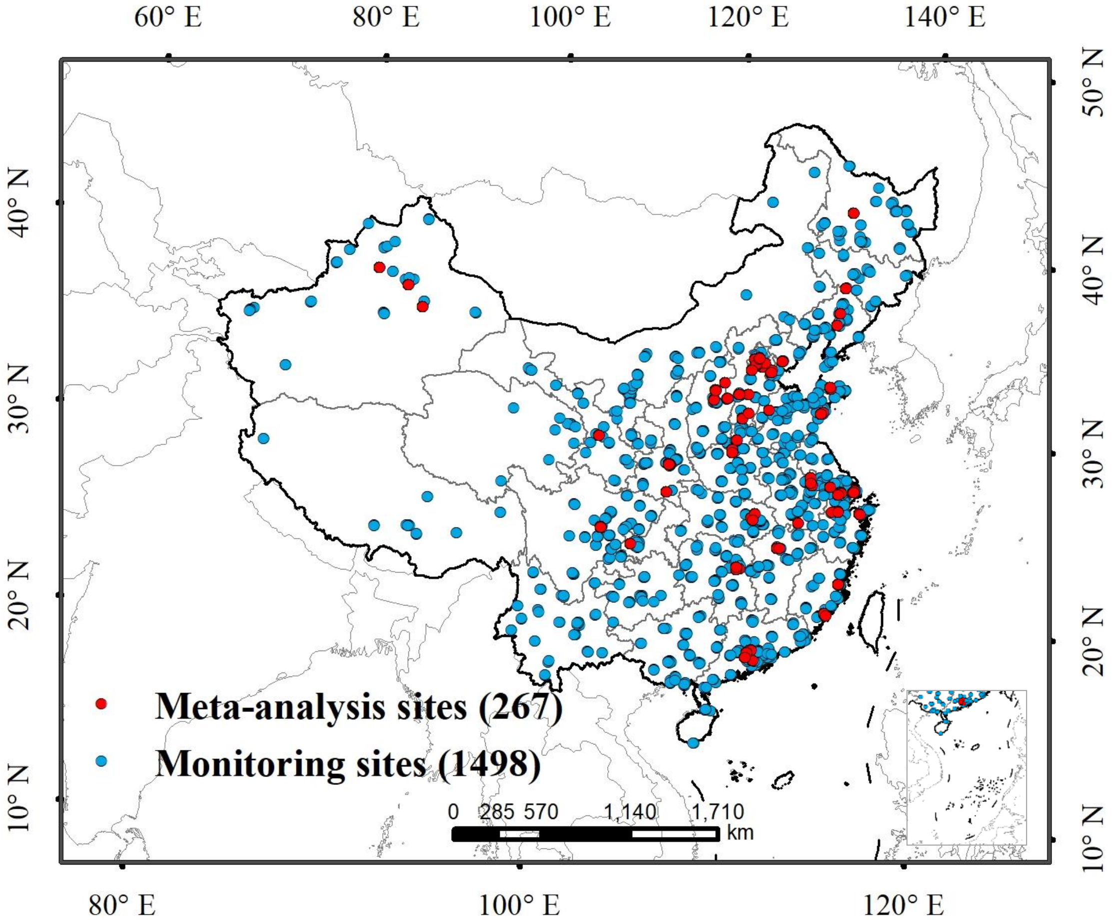

Figure S1. Spatial distribution of the 1498 monitoring sites (blue dots) and the 218 meta-analysis sites (red dots).

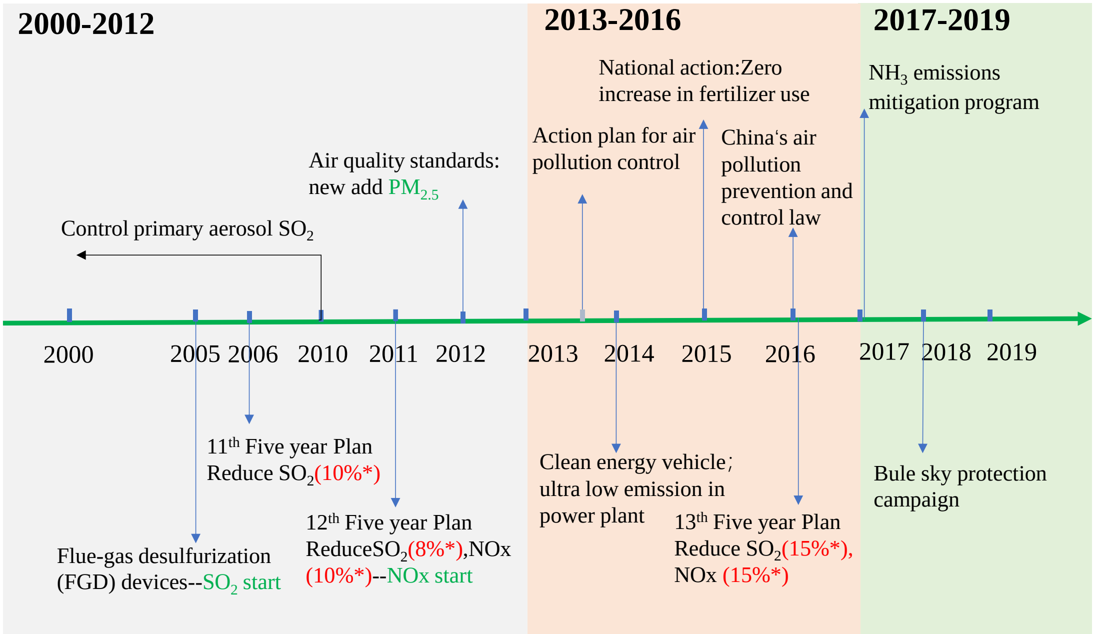

Figure S2. Timeline of policies to improve air quality in China. The green text indicates the start of control policies from the Chinese government for the pollutant highlighted; the * symbol and red text indicates the pollutant emission reduction target in the given 5-year plan. The different background colors denote the three different pollutant history periods (Periods I, II and III) described in the main text.

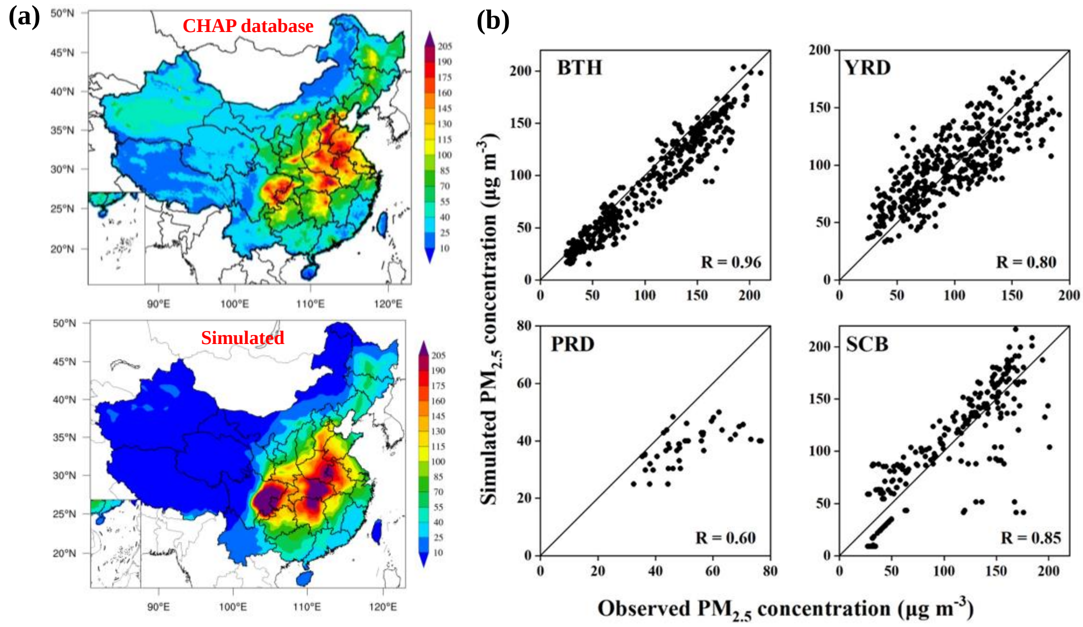

Figure S3. (a) Simulated and observed monthly mean $PM_{2.5}$ concentrations (μg m^{-3}) for January 2010. The observations are from the ChinaHighAirPollutants (CHAP, https://weijing-rs.github.io/product.html) database. (b) Scatter plots of simulated versus observed monthly means $PM_{2.5}$ concentration in the BTH, YRD, PRD, and SCB regions.

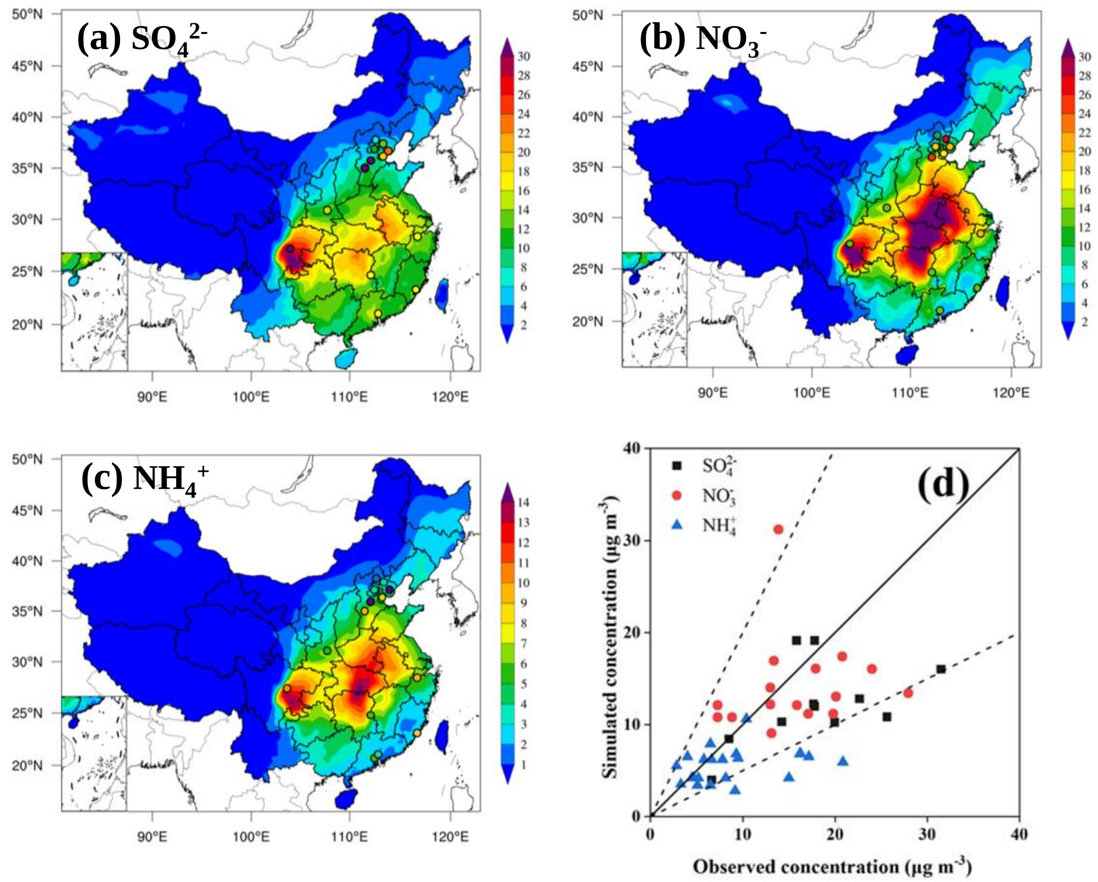

Figure S4. Overlay of observed (colored circles) and simulated (color map) monthly mean concentrations of (a) SO_4^{2-}, (b) NO_3^- and (c) NH_4^+ in January 2010. (d) scatter plot of simulated and observed concentrations of SO_4^{2-}, NO_3^- and NH_4^+. The dotted lines correspond to the 1:2 and 2:1 lines. The observations are collected from the literature (See Table S5).

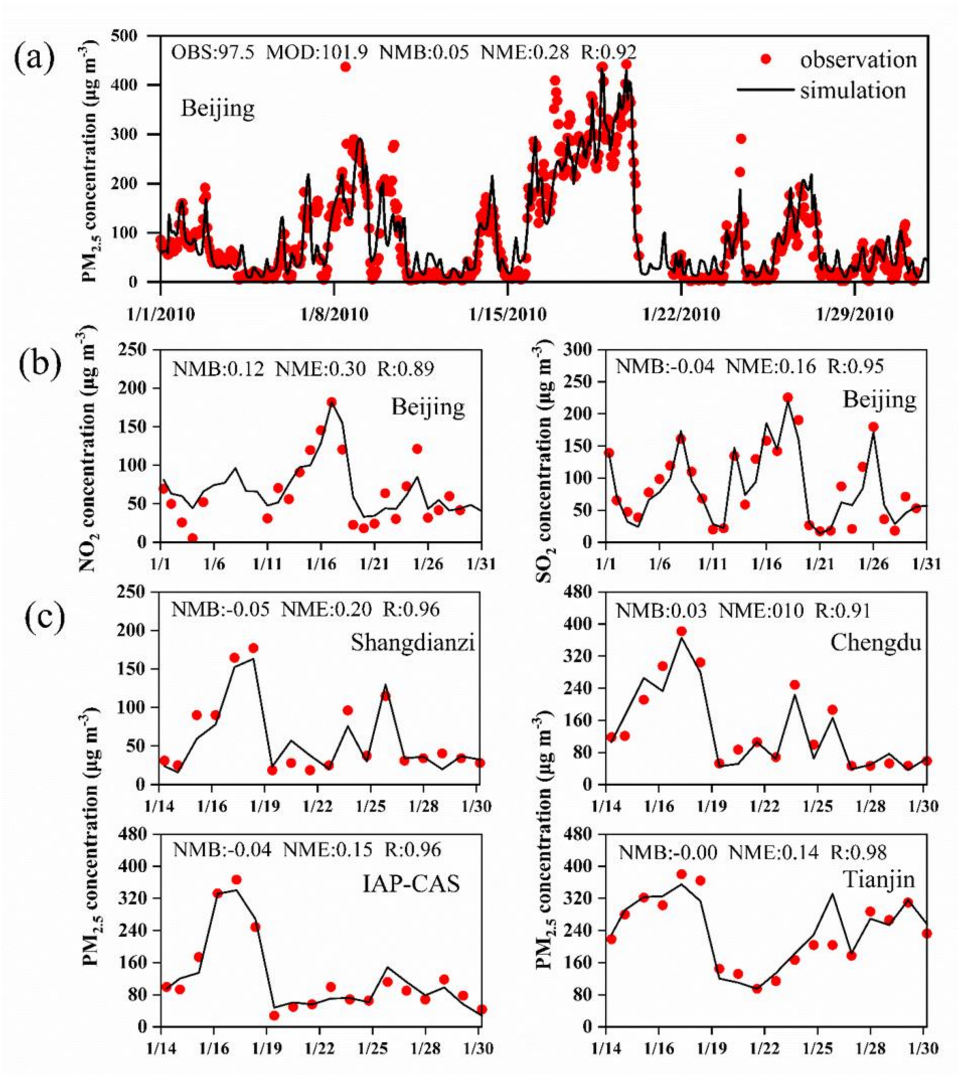

Figure S5. Time series of the observed (red dots) and simulated (black line) (a) hourly concentrations of $PM_{2.5}$ and (b) daily concentrations of NO_2 and SO_2 in January 2010 in Beijing; (c) daily concentrations of $PM_{2.5}$ during 14-30 January 2010 at monitoring sites in Shangdianzi, Chengdu, Institute of Atmospheric Physics, Chinese Academy of Sciences (IAP-CAS) and Tianjin. The normalized mean bias (NMB) normalized mean error (NME), and correlation coefficient (R) are given in the plots.

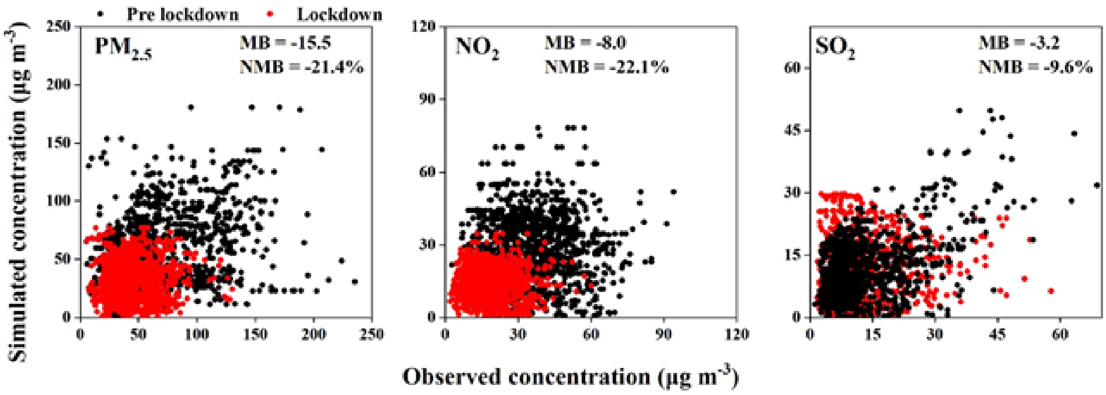

Figure S6. Scatter plots of CMAQ simulations versus surface observations for $PM_{2.5}$, NO_2, and SO_2 concentrations before the COVID-lockdown (black dots) and during the COVID-lockdown period (red dots).

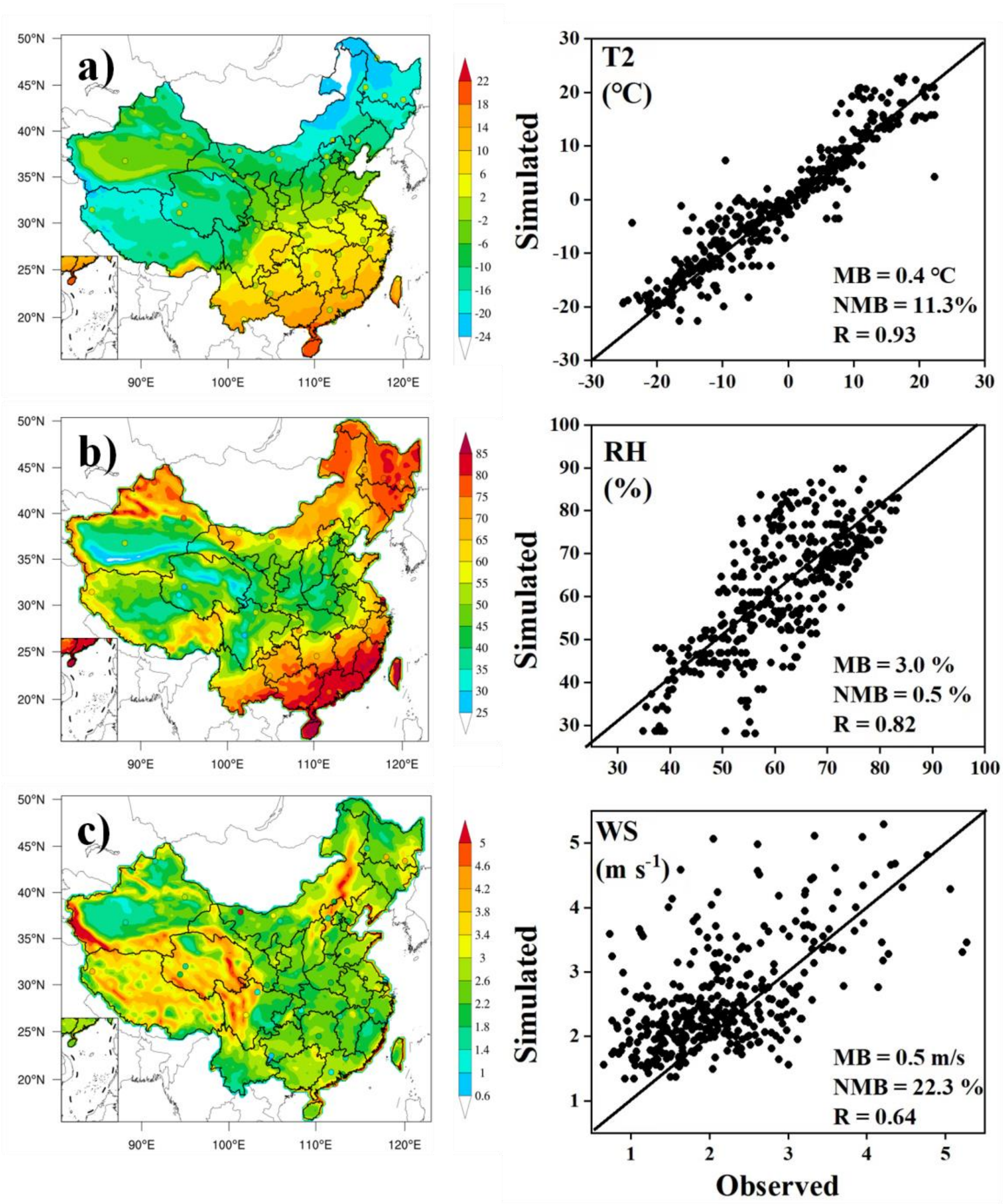

Figure S7. The left column shows simulated (shaded) and observed (dot) monthly-mean temperature at 2 m above the ground (T2) (a), wind speed (WS) (b), and (c) relative humidity (RH) for January 2010. The right column shows scatterplots of simulated versus observed T2, WS, RH at 400 monitoring sites in China. The value of correlation coefficients (*R*) is presented on each scatterplot.

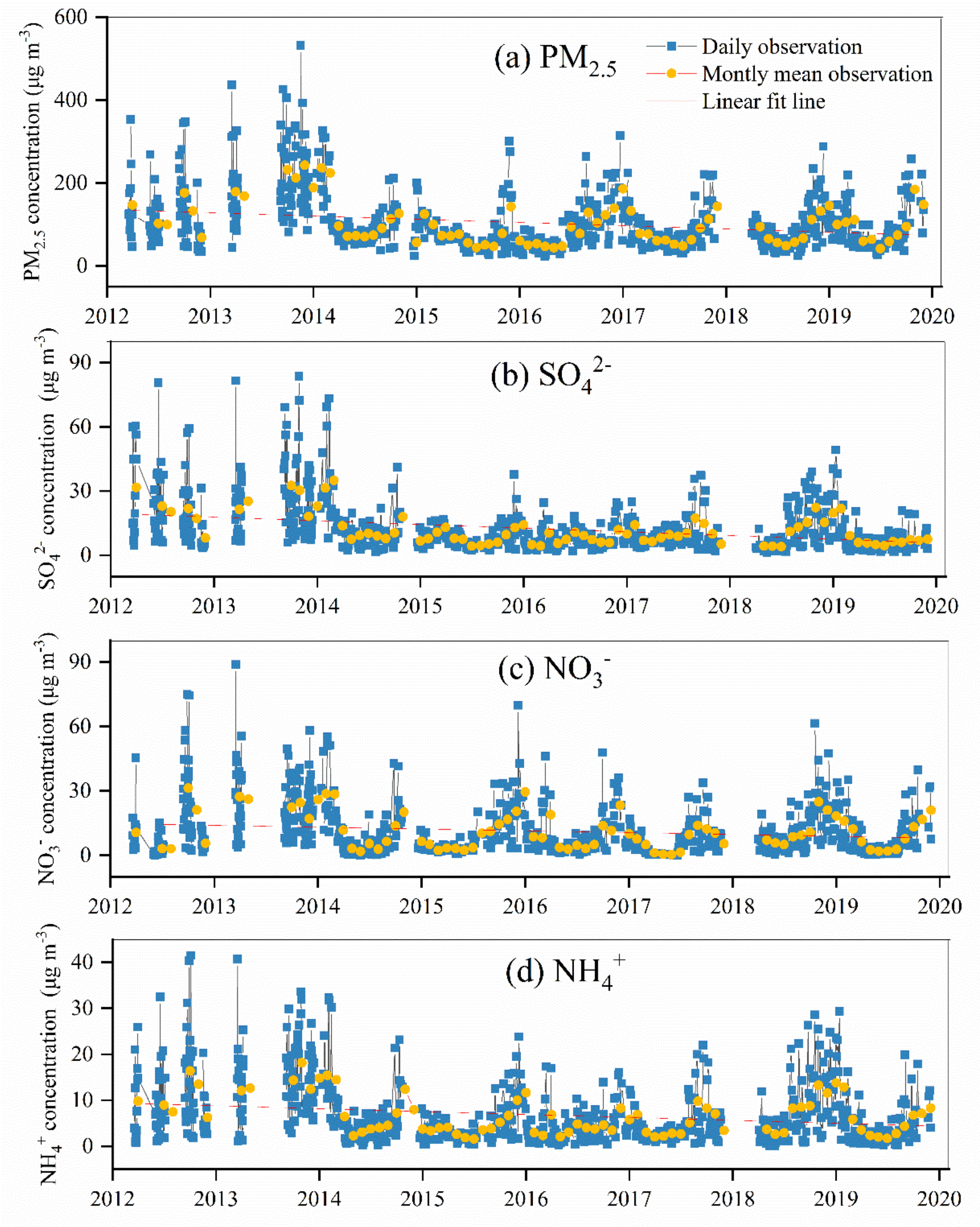

Figure S8. Daily and monthly concentration of (a) $PM_{2.5}$, (b) SO_4^{2-}, (c)NO_3^-, and (d) NH_4^+ in Quzhou in China during 2002-2019

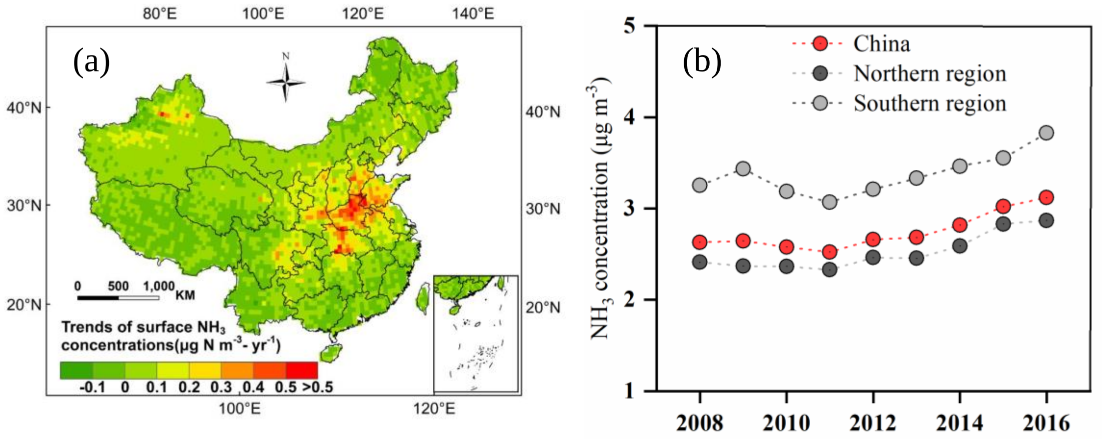

Figure S9. (a) Spatial patterns of trends between 2008 and 2016 in annual mean concentrations of NH_3. (b) Annual average ground-based measured NH_3 concentrations 2008-2016 across all of China and in northern and southern regions. Data for map (a) are from NH_3 satellite retrievals combining vertical profiles from Goddard Earth Observing System-Chemistry (GEOS-Chem).

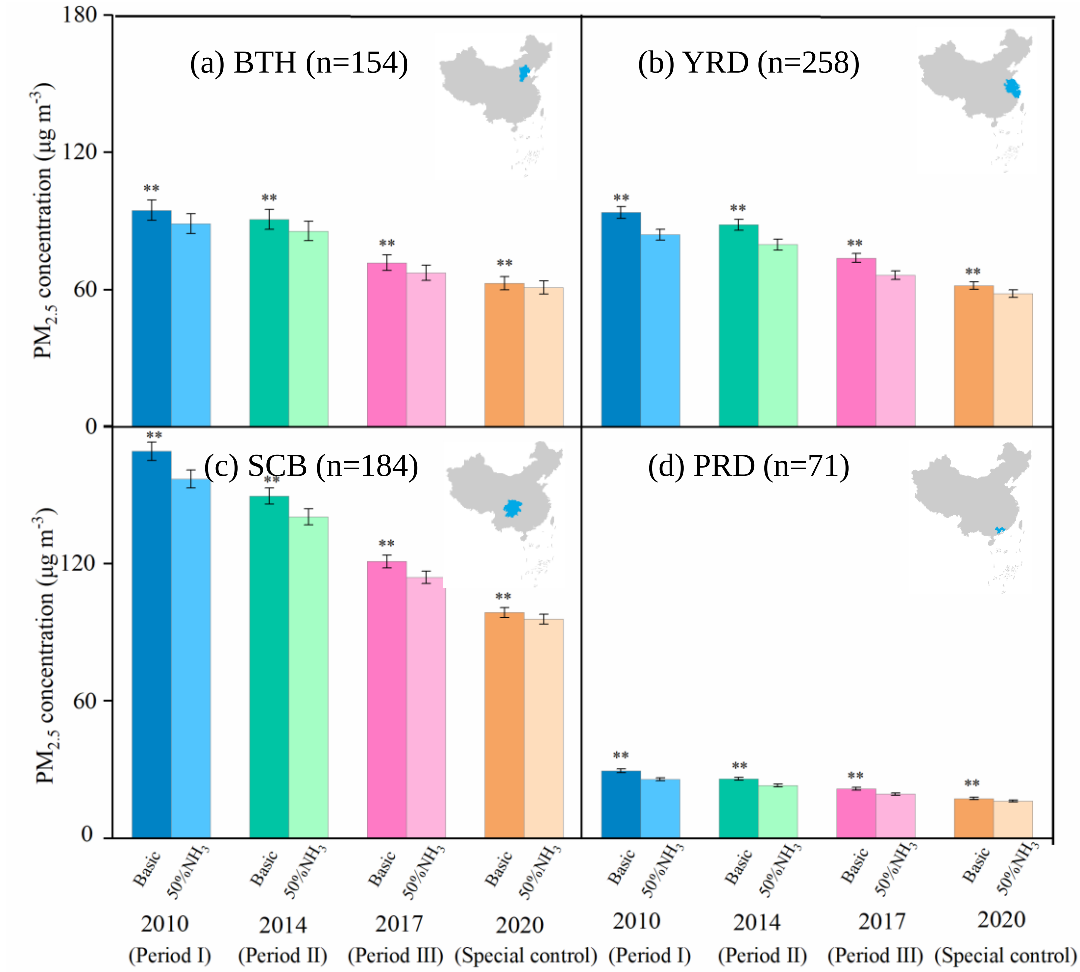

Figure S10. Simulated $PM_{2.5}$ concentrations (in μg m^{-3}) without (basic) and with 50% ammonia (NH_3) emissions reductions in January for the years 2010, 2014, 2017 and 2020 in four megacity clusters (BTH: Beijing-Tianjin-Hebei, YRD: Yangtze River Delta, SCB: Sichuan Basin, PRD: Pearl River Delta). Inset maps indicate the location of each region. ** denotes significant difference without and with 50% ammonia emission reductions (P <0.05). n is the number of calculated samples by grid extraction. Error bars are standard errors of means. (Period I (2000–2012), Period II (2013–2016), and Period III (2017–2019); Special control is the restrictions in economic activities and associated emissions during the COVID-19 lockdown period in 2020.)

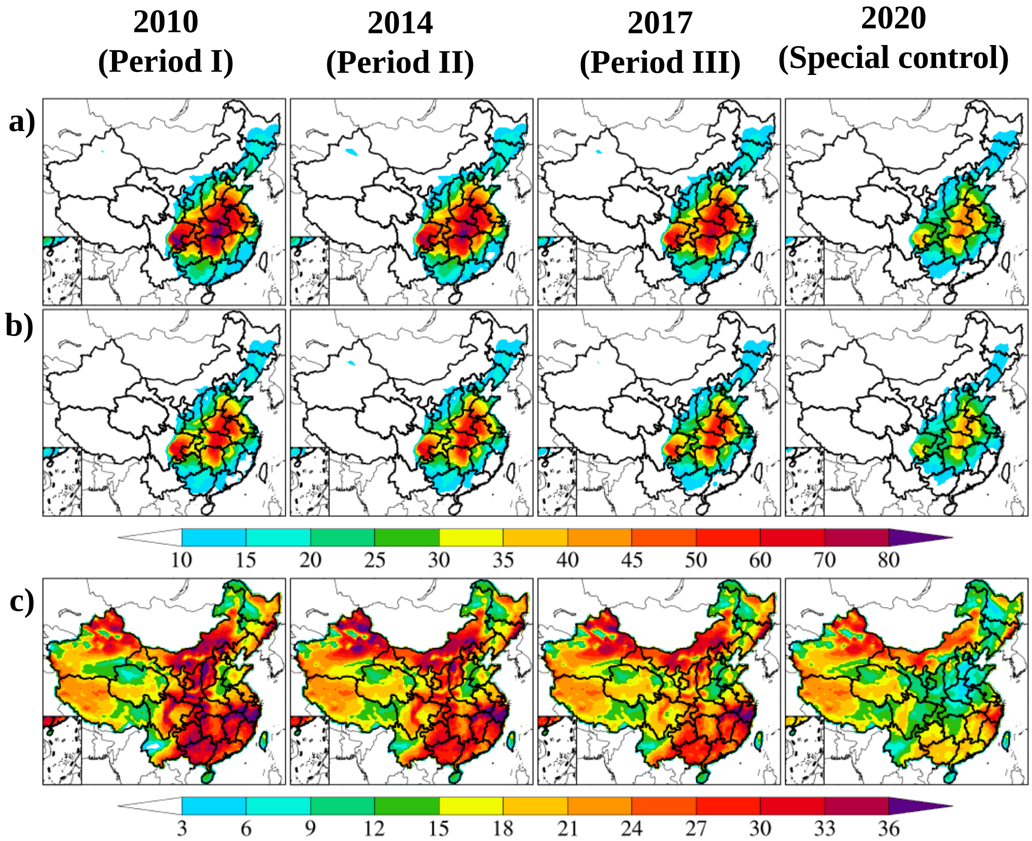

Figure S11. The spatial distributions of simulated SIA concentrations (in μg m^{-3}) without (a) and with (b) 50% ammonia emissions reduction for the years 2010, 2014, 2017 and 2020. The % decreases in SIA concentrations in each year for the simulations with the emissions reductions are shown in row (c). (Period I (2000–2012), Period II (2013–2016), and Period III (2017–2019); Special control is the restrictions in economic activities and associated emissions during the COVID-19 lockdown period in 2020.)

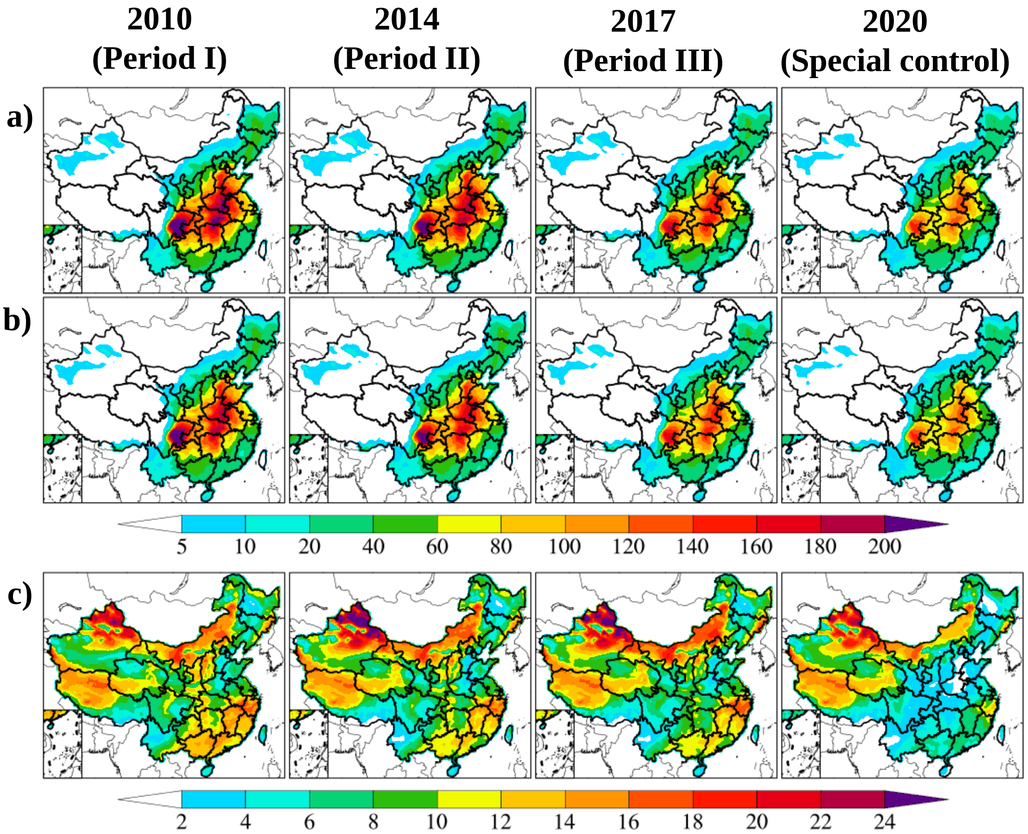

Figure S12. The spatial distributions of simulated $PM_{2.5}$ concentrations (in μg m^{-3}) without (a) and with (b) 50% ammonia emissions reduction for the years 2010, 2014, 2017 and 2020. The % decreases in $PM_{2.5}$ concentrations in each year for the simulations with the emissions reductions are shown in row (c). (Period I (2000–2012), Period II (2013–2016), and Period III (2017–2019); Special control is the restrictions in economic activities and associated emissions during the COVID-19 lockdown period in 2020.)

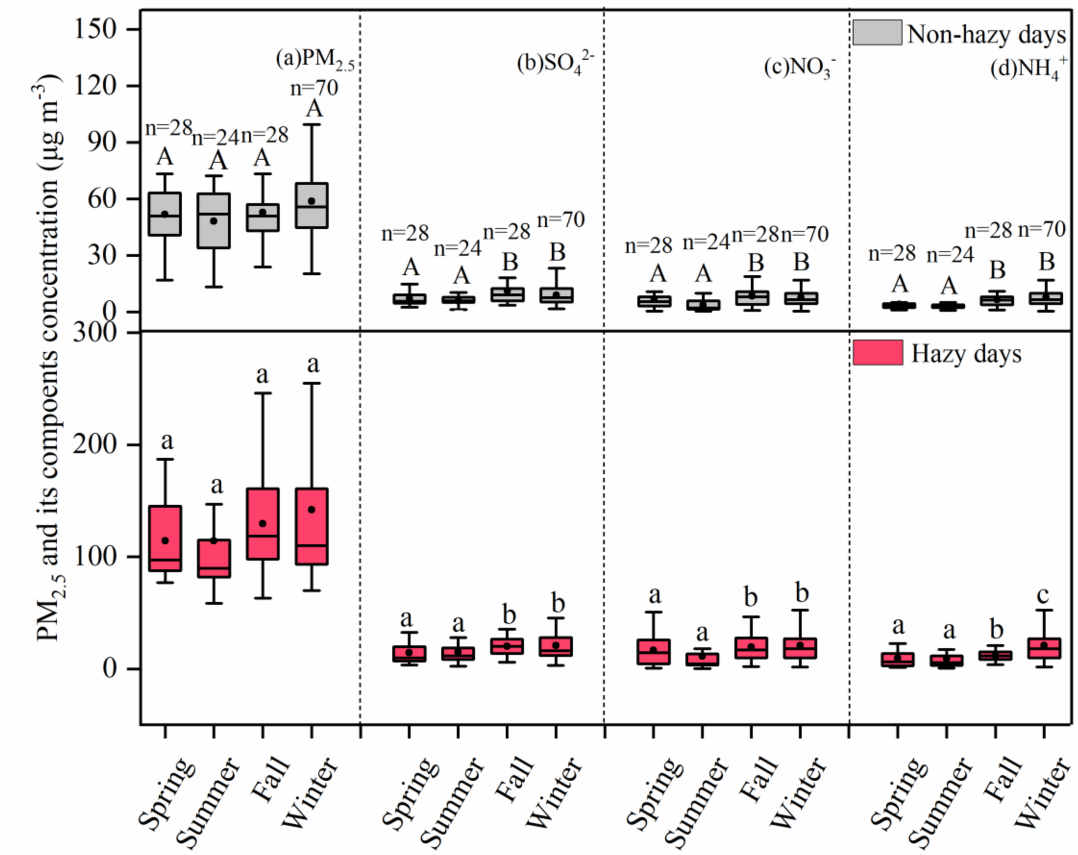

Figure S13. Comparisons of observed concentrations of (a) $PM_{2.5}$, (b) SO_4^{2-}, (c) NO_3^-, and (d) NH_4^+ between non-hazy and hazy days in Spring, Summer, Fall, and Winter during 2000-2019. Bars with different letters denote significant differences among the three periods ($P < 0.05$) (upper and lowercase letters for non-hazy and hazy days, respectively). The upper and lower boundaries of the boxes represent the 75th and 25th percentiles; the line within the box represents the median value; the whiskers above and below the boxes represent the 90th and 10th percentiles; the point within the box represents the mean value. Comparison of the pollutants among the three-periods using Kruskal-Wallis and Dunn's test. The n represents independent sites; more detail on this is presented in Section 2.2.

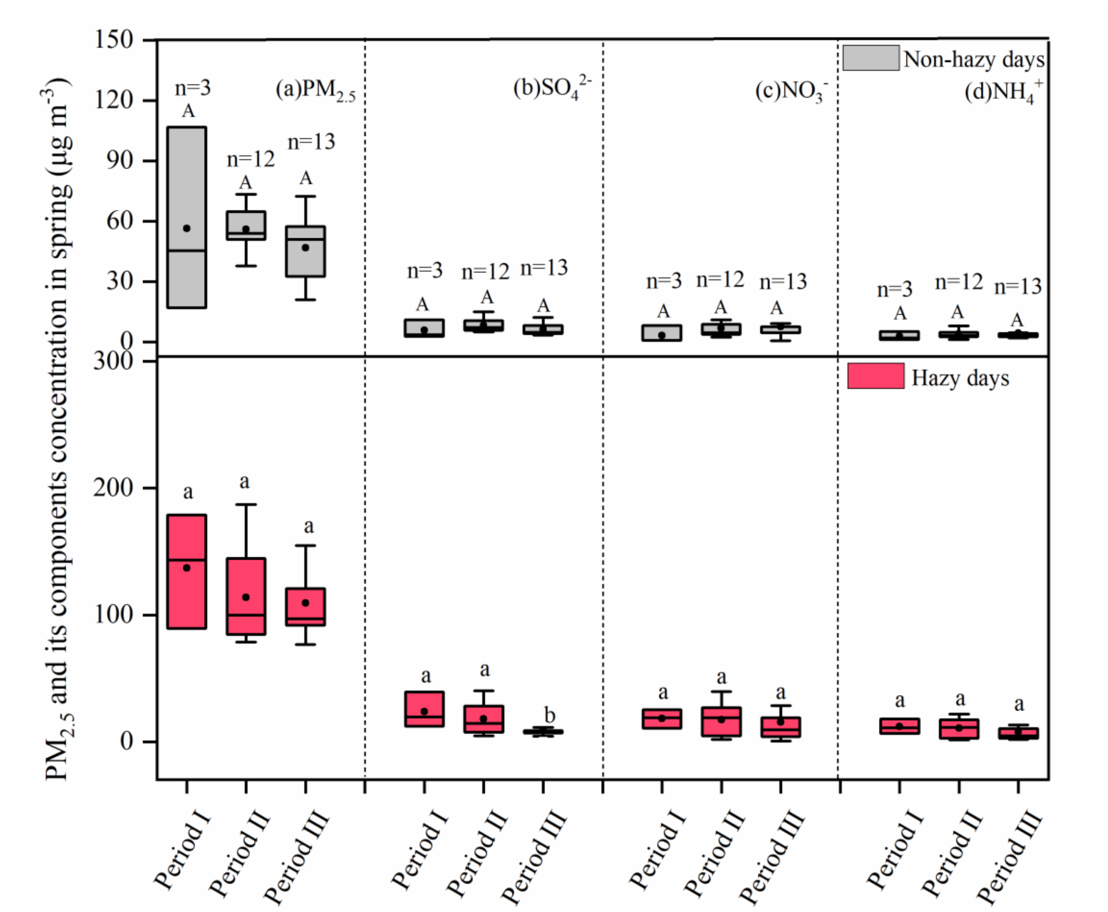

Figure S14. Comparisons of observed concentrations of (a) $PM_{2.5}$, (b) SO_4^{2-}, (c) NO_3^-, and (d) NH_4^+ between non-hazy and hazy days in Spring in Period I (2000–2012), Period II (2013–2016), and Period III (2017–2019). Bars with different letters denote significant differences among the three periods ($P < 0.05$) (upper and lowercase letters for non-hazy and hazy days, respectively). The upper and lower boundaries of the boxes represent the 75th and 25th percentiles; the line within the box represents the median value; the whiskers above and below the boxes represent the 90th and 10th percentiles; the point within the box represents the mean value. Comparison of the pollutants among the three-periods using Kruskal-Wallis and Dunn's test. The n represents independent sites; more detail on this is presented in Section 2.2.

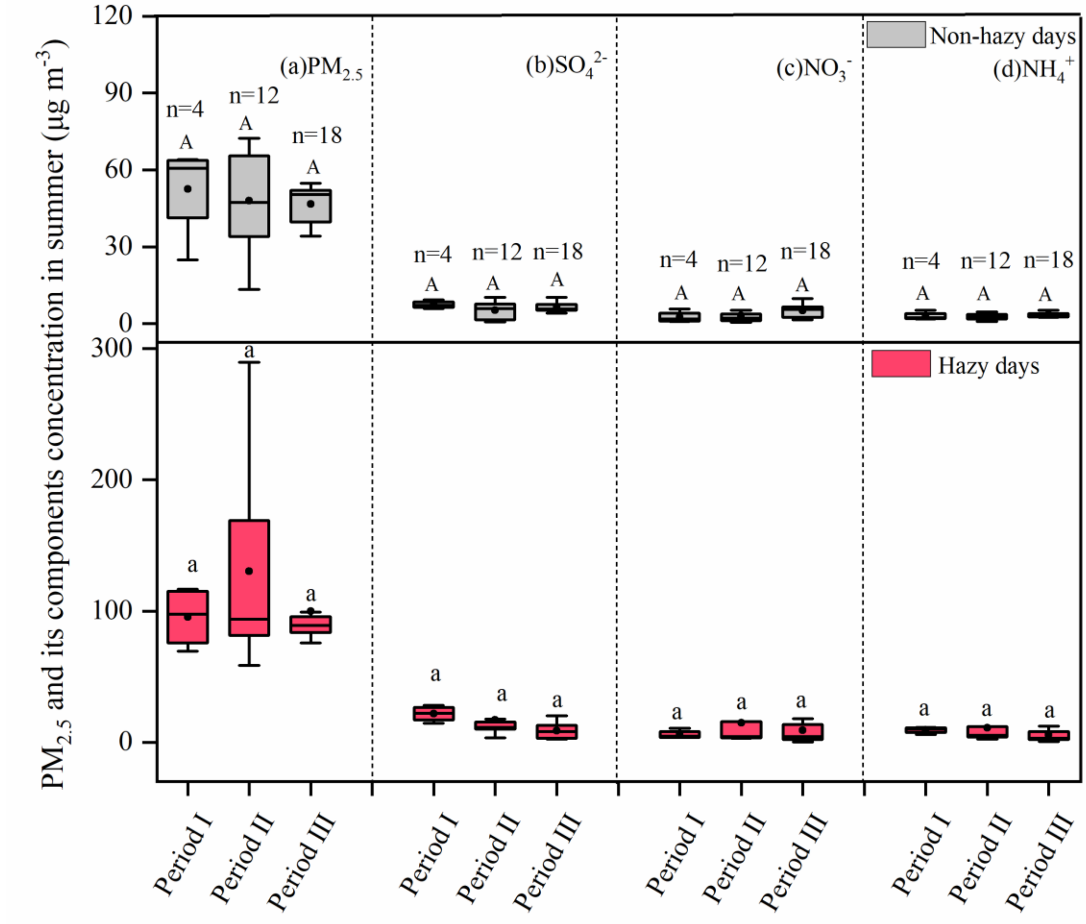

Figure S15. Comparisons of observed concentrations of (a) $PM_{2.5}$, (b) SO_4^{2-}, (c) NO_3^-, and (d) NH_4^+ between non-hazy and hazy days in Summer in Period I (2000–2012), Period II(2013–2016), and Period III(2017–2019). Bars with different letters denote significant differences among the three periods (P<0.05) (upper and lowercase letters for non-hazy and hazy days, respectively). The upper and lower boundaries of the boxes represent the 75th and 25th percentiles; the line within the box represents the median value; the whiskers above and below the boxes represent the 90th and 10th percentiles; the point within the box represents the mean value. Comparison of the pollutants among the three-periods using Kruskal-Wallis and Dunn's test. The n represents independent sites; more detail on this is presented in Section 2.2.

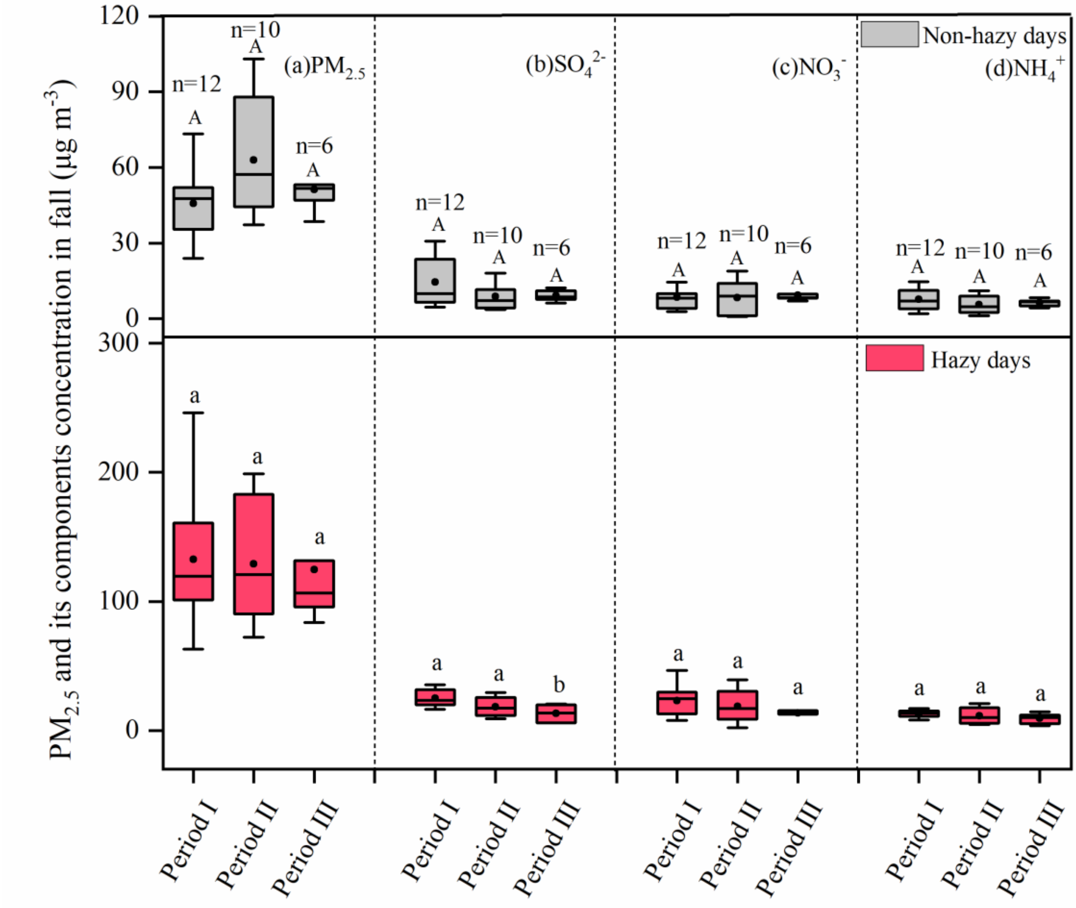

Figure S16. Comparisons of observed concentrations of (a) $PM_{2.5}$, (b) SO_4^{2-}, (c) NO_3^-, and (d) NH_4^+ between non-hazy and hazy days in Fall in Period I (2000–2012), Period II (2013–2016), and Period III (2017–2019). Bars with different letters denote significant differences among the three periods (P <0.05) (upper and lowercase letters for non-hazy and hazy days, respectively). The upper and lower boundaries of the boxes represent the 75th and 25th percentiles; the line within the box represents the median value; the whiskers above and below the boxes represent the 90th and 10th percentiles; the point within the box represents the mean value. Comparison of the pollutants among the three-periods using Kruskal-Wallis and Dunn's test. The n represents independent sites; more detail on this is presented in Section 2.2.

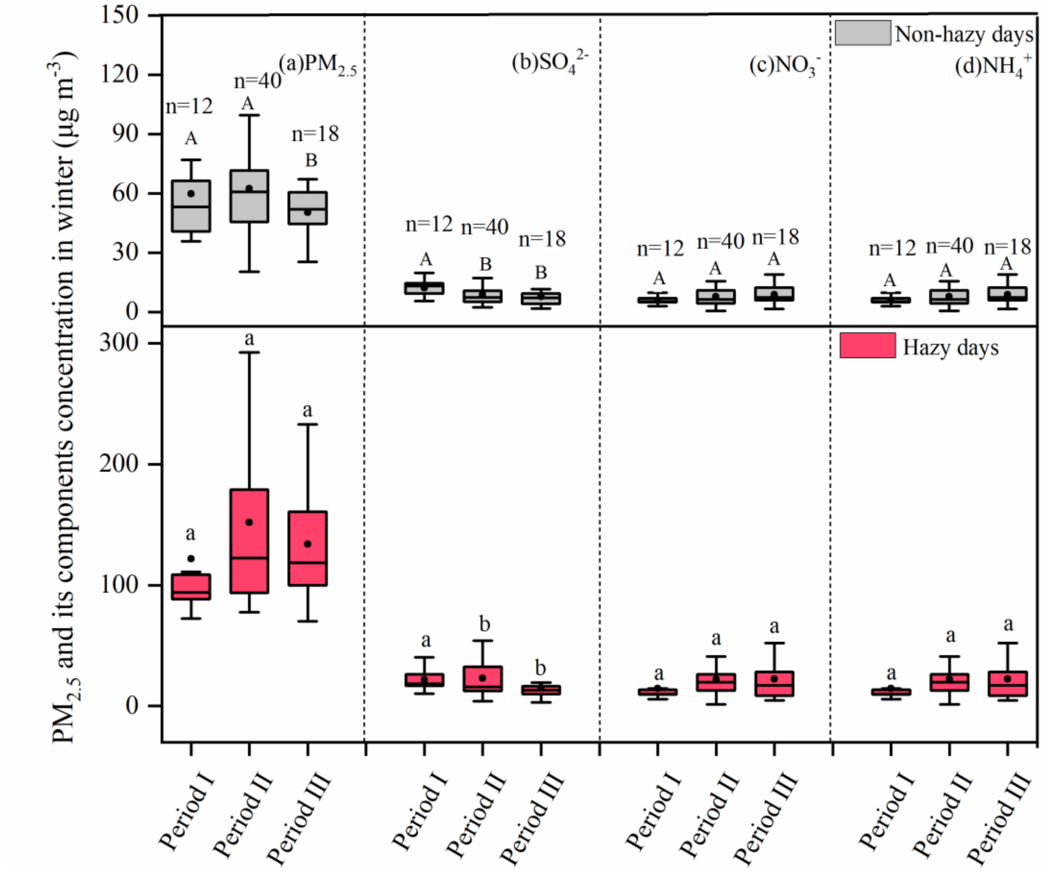

Figure S17. Comparisons of observed concentrations of (a) $PM_{2.5}$, (b) SO_4^{2-}, (c) NO_3^-, and (d) NH_4^+ between non-hazy and hazy days in Winter in Period I (2000–2012), Period II (2013–2016), and Period III (2017–2019). Bars with different letters denote significant differences among the three periods (P<0.05) (upper and lowercase letters for non-hazy and hazy days, respectively). The upper and lower boundaries of the boxes represent the 75th and 25th percentiles; the line within the box represents the median value; the whiskers above and below the boxes represent the 90th and 10th percentiles; the point within the box represents the mean value. Comparison of the pollutants among the three-periods using Kruskal-Wallis and Dunn's test. The n represents independent sites; more detail on this is presented in Section 2.2.

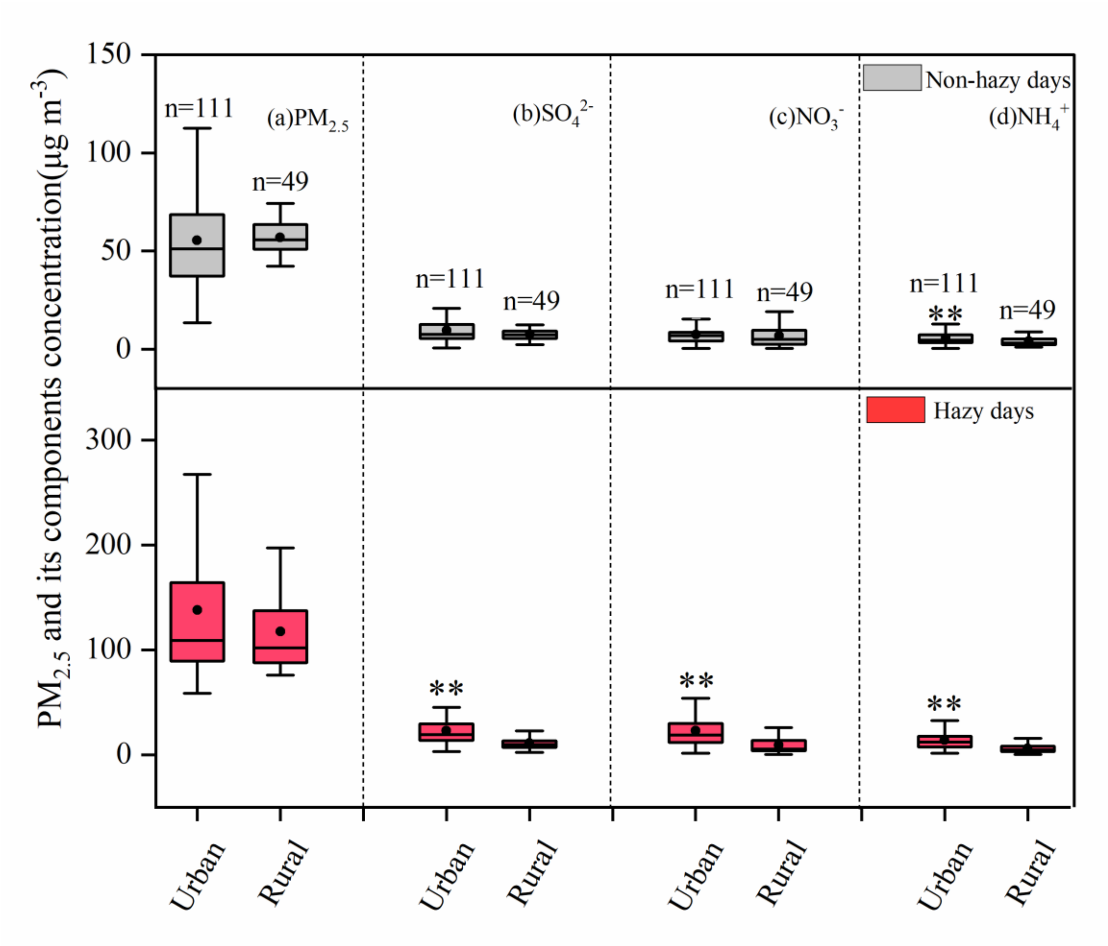

Figure S18. Comparisons of observed concentrations of (a) $PM_{2.5}$, (b) SO_4^{2-}, (c) NO_3^-, and (d) NH_4^+ between non-hazy and hazy days in Urban and Rural sites during 2000-2019. Bars with ** denote significant differences among the three periods (P<0.05) (upper and lowercase letters for non-hazy and hazy days, respectively). The upper and lower boundaries of the boxes represent the 75th and 25th percentiles; the line within the box represents the median value; the whiskers above and below the boxes represent the 90th and 10th percentiles; the point within the box represents the mean value. Comparison of the pollutants among the three-periods using Kruskal-Wallis and Dunn's test. The *n* represents independent sites; more detail on this is presented in Section 2.2.

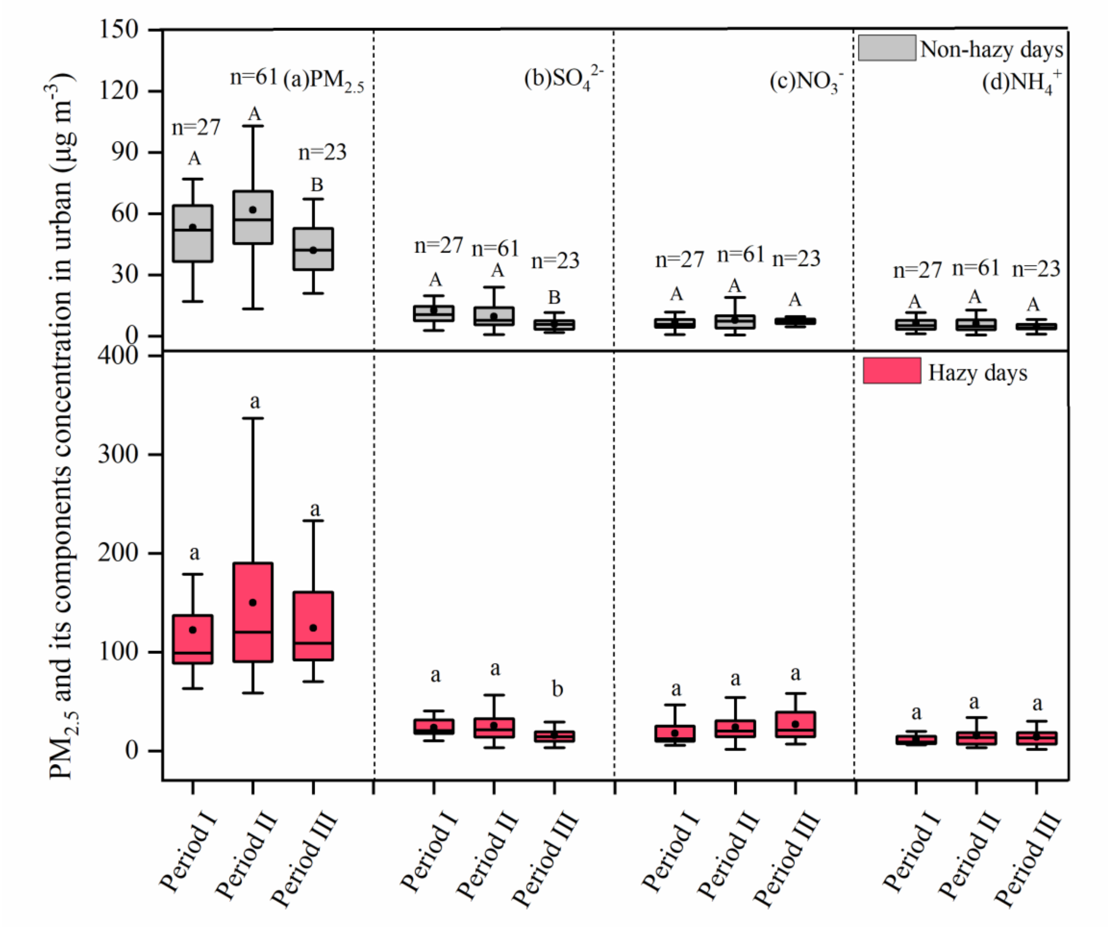

Figure S19. Comparisons of observed concentrations of (a) $PM_{2.5}$, (b) SO_4^{2-}, (c) NO_3^-, and (d) NH_4^+ between non-hazy and hazy days in urban sites in Period I (2000–2012), Period II (2013–2016), and Period III (2017–2019). Bars with different letters denote significant differences among the three periods (P<0.05) (upper and lowercase letters for non-hazy and hazy days, respectively). The upper and lower boundaries of the boxes represent the 75th and 25th percentiles; the line within the box represents the median value; the whiskers above and below the boxes represent the 90th and 10th percentiles; the point within the box represents the mean value. Comparison of the pollutants among the three-periods using Kruskal-Wallis and Dunn's test. The n represents independent sites; more detail on this is presented in Section 2.2.

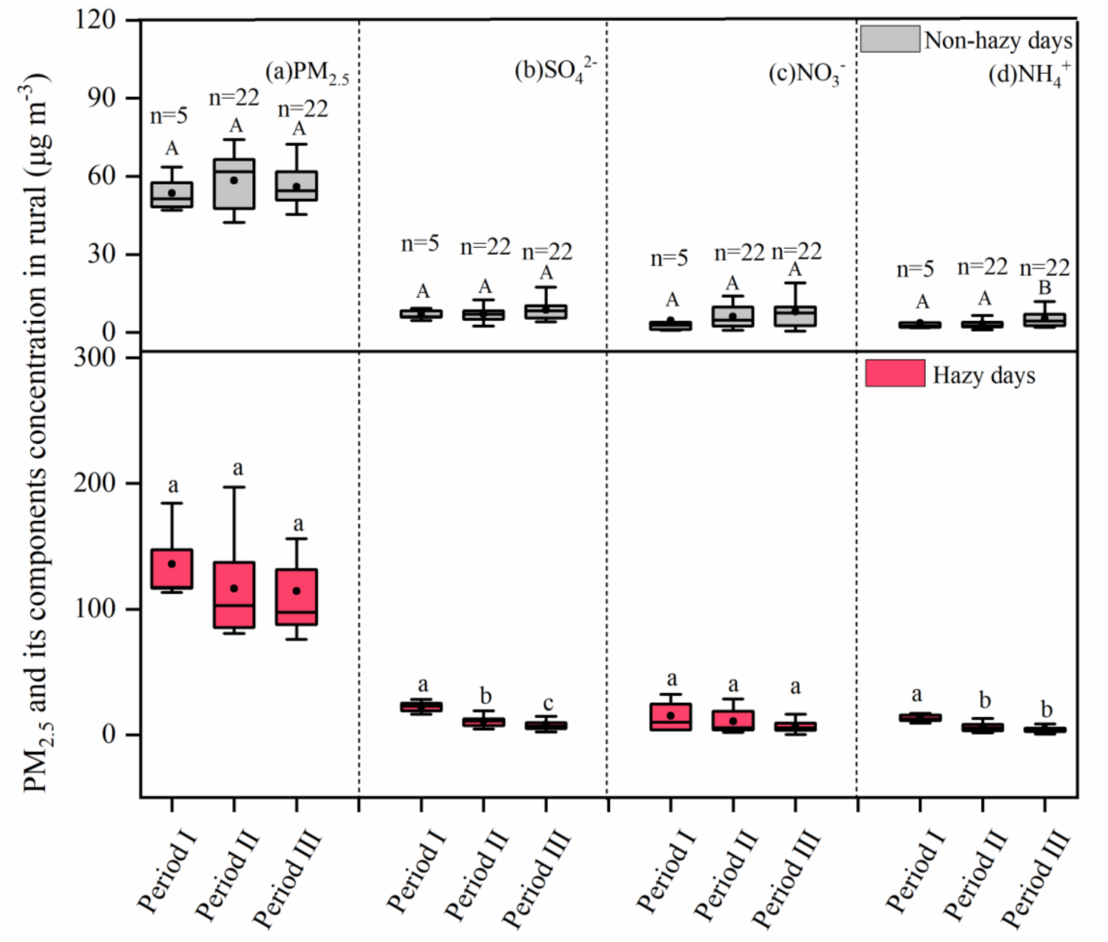

Figure S20. Comparisons of observed concentrations of (a) $PM_{2.5}$, (b) SO_4^{2-}, (c) NO_3^-, and (d) NH_4^+ between non-hazy and hazy days in rural sites in Period I (2000–2012), Period II (2013–2016), and Period III (2017–2019). Bars with different letters denote significant differences among the three periods (P<0.05) (upper and lowercase letters for non-hazy and hazy days, respectively). The upper and lower boundaries of the boxes represent the 75th and 25th percentiles; the line within the box represents the median value; the whiskers above and below the boxes represent the 90th and 10th percentiles; the point within the box represents the mean value. Comparison of the pollutants among the three-periods using Kruskal-Wallis and Dunn's test. The n represents independent sites; more detail on this is presented in Section 2.2.

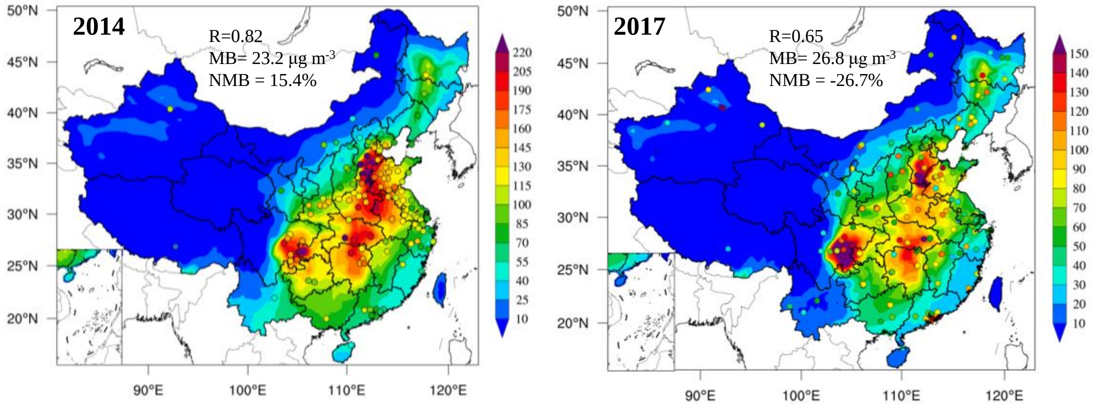

Figure S21. Overlay of observed (colored circles) and simulated (color map) monthly concentrations of $PM_{2.5}$ in January 2014 and 2017.

Table S1. Summary of number of measurment sites from different databases assembled from peer-reviewed publications and used for analyses in the present study of $PM_{2.5}$ component concentrations, NS, NSN, SOR, and NOR. The details of information in Supporting Material Dataset. NS is the slope of the regression equation between $[NH_4^+]$ and $[SO_4^{2-}]$, NSN is the slope of the regression equation between $[NH_4^+]$ and $[SO_4^{2-} + NO_3^-]$, SOR is sulfur oxidation ratio, and NOR is nitrogen oxidation ratio.

	No. of measurement sites	N_{f_s} [a]	$5n + 10$ [b]
OC	84	531290	430
EC	101	396171	515
SO_4^{2-}	151	2385388	765
NO_3^-	175	4542962	885
Cl^-	105	886197	535
F^-	26	1587	140
NH_4^+	166	4026300	840
Na^+	82	343318	420
K^+	91	523882	465
Ca^{2+}	75	88883	385
Mg^{2+}	68	—	350
NS	145	—	735
NSN	144	—	730
SOR	38	—	200
NOR	33	—	175

Note: [a] N_{f_s} is Rosenberg's fail safe-numbers, calculated to assess the robustness of findings on $PM_{2.5}$. [b] n is the number of sites.

Table S2. Anthropogenic emissions of SO_2 in January of 2010, 2014, 2017 and 2020, and the percentage decreases in SO_2 emissions between successive pairs of years.

	2010	2014	2017	2020	**2014-2010**	**2017-2014**	**2020-2017**
	Tonne	Tonne	Tonne	Tonne	%	%	%
Beijing	20410	10899	4051	2998	-47	-63	-26
Tianjin	29000	22111	9042	7233	-24	-59	-20
Hebei	183194	146125	70877	59536	-20	-51	-16
Shanxi	193721	151346	111566	89253	-22	-26	-20
Inner Mongolia	158304	121932	66986	56938	-23	-45	-15
Liaoning	97766	77459	41043	29551	-21	-47	-28
Jilin	44399	34995	23713	18259	-21	-32	-23
Heilongjiang	44491	43441	28536	20832	-2	-34	-27
Shanghai	43016	28112	14390	8346	-35	-49	-42
Jiangsu	113216	69162	27388	20267	-39	-60	-26
Zhejiang	52789	35704	17846	12671	-32	-50	-29
Anhui	43583	30433	15703	12248	-30	-48	-22
Fujian	37907	19804	13537	9476	-48	-32	-30
Jiangxi	40179	28746	14362	11346	-28	-50	-21
Shandong	244765	178189	84499	63374	-27	-53	-25
Henan	125492	72270	34617	27002	-42	-52	-22
Hubei	182208	112715	69204	53287	-38	-39	-23
Hunan	92142	90407	68003	51002	-2	-25	-25
Guangdong	75644	46140	35595	23849	-39	-23	-33
Guangxi	68551	43141	22565	16247	-37	-48	-28
Hainan	4008	4790	3933	2950	20	-18	-25
Chongqing	120968	67877	35101	23868	-44	-48	-32
Sichuan	113414	75375	37241	27186	-34	-51	-27
Guizhou	191009	181314	111426	83569	-5	-39	-25
Yunnan	66724	54142	33106	24830	-19	-39	-25
Tibet	60	66	97	82	10	47	-15
Shaanxi	105817	76442	40069	32856	-28	-48	-18
Gansu	38708	23976	19749	16590	-38	-18	-16
Qinghai	4778	5594	4310	3362	17	-23	-22
Ningxia	28415	24767	20062	15247	-13	-19	-24
Xinjiang	44162	45561	24929	21190	3	-45	-15
China	2608842	1923034	1103546	845445	-26	-43	-23

Note**:** SO_2 emissions were provided by the Multi-resolution Emission Inventory (MEIC) (http://meicmodel.org) for the years 2010, 2014 and 2017. The SO_2 emissions of 2020 are based on 2017 MEIC as a case of special control following Huang et al. (2021) approach.

Table S3. Anthropogenic emissions of NO_x in January of 2010, 2014, 2017 and 2020, and the percentage decreases in NOx emissions between successive pairs of years.

	2010	2014	2017	2020	**2014-2010**	**2017-2014**	**2020-2017**
	Tonne	Tonne	Tonne	Tonne	%	%	%
Beijing	32325	27223	24931	13712	-16	-8	-45
Tianjin	33978	37380	30435	18870	10	-19	-38
Hebei	177625	167812	148367	81602	-6	-12	-45
Shanxi	106872	95243	82741	49645	-11	-13	-40
Inner Mongolia	129645	120068	111328	79043	-7	-7	-29
Liaoning	113719	112970	104711	62826	-1	-7	-40
Jilin	61173	58140	60342	36808	-5	4	-39
Heilongjiang	77226	81565	74725	47077	6	-8	-37
Shanghai	45395	32961	31539	16400	-27	-4	-48
Jiangsu	153102	142730	131740	65870	-7	-8	-50
Zhejiang	95531	75644	71440	35720	-21	-6	-50
Anhui	86796	87662	78304	34454	1	-11	-56
Fujian	47505	41396	46573	22821	-13	13	-51
Jiangxi	39804	39120	34918	16411	-2	-11	-53
Shandong	222442	201757	177591	88796	-9	-12	-50
Henan	137270	126230	105735	45466	-8	-16	-57
Hubei	76893	69558	59338	26702	-10	-15	-55
Hunan	67695	61721	56416	27644	-9	-9	-51
Guangdong	109844	87421	86116	43058	-20	-1	-50
Guangxi	47006	42915	35959	17980	-9	-16	-50
Hainan	6813	7437	7689	4306	9	3	-44
Chongqing	37763	36995	32855	15442	-2	-11	-53
Sichuan	82543	80131	69170	34585	-3	-14	-50
Guizhou	50554	43218	33805	20621	-15	-22	-39
Yunnan	52995	42479	36285	17779	-20	-15	-51
Tibet	2428	2337	3625	2357	-4	55	-35
Shaanxi	58296	56807	48598	26729	-3	-14	-45
Gansu	37634	31398	28059	14871	-17	-11	-47
Qinghai	7872	10535	8907	4810	34	-15	-46
Ningxia	23645	27323	27936	17879	16	2	-36
Xinjiang	42625	62771	48156	31301	47	-23	-35
China	2265015	2110946	1898332	1021583	-7	-10	-46

Note**:** NO_x emissions were provided by the Multi-resolution Emission Inventory (MEIC) (http://meicmodel.org) for the years 2010, 2014 and 2017. The NO_x emissions of 2020 are based on 2017 MEIC as a case of special control following Huang et al. (2021) approach.

Table S4. Control options for NH_3 emissions reductions with their corresponding estimated percentage emissions reductions (reduction efficiency).

Abatement option	Application processes	Reduction efficiency
Avoiding over-fertilization	Synthetic fertilizer application	>20%
Deep application of fertilizers	Synthetic fertilizer application	~50%
Low crude protein feed	Whole manure management chain	10-40%
Using deep litter in floor and regular washing	Manure in house	20-50%
Covering solid and slurry manure	Manure storage	>60%
Incorporation or plough after spreading	Field application of manure	40-80%
All	**NH_3 emissions for all China**	**30-50%**

Note: The NH_3 emissions control options and corresponding emissions reduction efficiency are from Liu et al. (2019). The feasible control options can reduce China's NH_3 emissions by 30-50% based on the PKU-NH_3 emission model.

Table S5. Monthly mean concentration of SO_4^{2-}, NO_3^-, and NH_4^+ in January in 2010.

ID	City	Lat	Lon	SO_4^{2-} (μg m^{-3})	NO_3^- (μg m^{-3})	NH_4^+ (μg m^{-3})	Reference
1	Guangzhou	113.4	27.1	17.8	13	6.5	(Tao et al., 2014)
2	Beijing	116.3	39.9	8.5	7.3	4.7	(Zhang et al., 2012)
3	Beijing	116.3	40.0	8.5	7.3	4.5	(Zhang et al., 2012)
4	Beijing	116.4	40.0	14.23	17.09	5.21	(Cao et al., 2014)
5	Beijing	116.7	40.9	6.64	8.84	2.83	(Zhang et al., 2012)
6	Guangzhou	113.5	23.2	17.8	13	3.3	(Tao et al., 2014)
7	Xiamen	118.1	24.6	17.67	13.15	9.17	(Zhang et al., 2012)
8	Beijing	116.4	40.0	15.8	15.9	8.2	(Pan et al., 2012)
9	Baoding	115.5	38.9	37.6	24.0	16.3	(Pan et al., 2012)
10	Tangshan	118.2	39.6	22.7	20.1	20.8	(Pan et al., 2012)
11	Tianjin	117.2	39.1	20.0	17.9	6.6	(Pan et al., 2012)
12	Xinglong	117.6	40.4	31.5	28.0	17.2	(Pan et al., 2012)

Table S6 Simulated SIA concentrations (in μg m^{-3}) with (basic) and 50% ammonia (NH_3) emissions reductions in January for years 2010, 2014, 2017, and 2020 in four megacity clusters.

	2010 (Period I)		2014 (Period II)		2017 (Period III)		2020 (Special control)	
	Base	50%NH_3	Base	50%NH_3	Base	50%NH_3	Base	50%NH_3
BTH	29.9±1.2	24.0±1.1	29.9±1.2	24.4±1.1	27.8±1.1	23.1±1.0	21.6±0.8	19.6±0.8
YRD	42.7±0.9	31.6±0.8	41.5±0.9	31.1±0.8	37.8±0.9	28.8±0.8	26.9±0.5	22.6±0.5
SCB	57.8±1.2	43.5±1.1	52.9±1.0	41.4±1.0	44.5±0.8	35.9±0.8	28.8±0.5	25.2±0.5
PRD	13.9±0.5	10.0±0.3	11.9±0.4	8.7±0.3	10.3±0.4	7.5±0.3	7.2±0.2	5.9±0.2

Note: The value is mean ± standard errors of means. (Period I (2000–2012), Period II (2013–2016), and Period III (2017–2019); Special control is the restrictions in economic activities and associated emissions during the COVID-19 lockdown period in 2020. BTH: Beijing-Tianjin-Hebei, YRD: Yangtze River Delta, SCB: Sichuan Basin, PRD: Pearl River Delta).

Table S7. The effectiveness of potential end-of pipe controls on SO_2 and NO_x emissions reductions for different production sectors (unit: %).

Sector	SO_2	NO_x
Electric	30	31
Industry - building materials	45	59
Industry - boiler	24	7
Industry - steel	—	3
Building	2	—

Note: The effectiveness of potential end-of pipe controls on SO_2 and NO_x emissions reductions for different production sectors from Xing et al. (2021). GetData Graph Digitizer (Version 2.25, http://www.getdatagraph-digitizer.com) was used to digitize the % effectiveness of SO_2 and NO_x from figures.

References

Cao, J. J.: $PM_{2.5}$ and the environment in China. China science publishing & media LTD. 9787030403810, 2014.

Huang, X., Ding, A.J, Gao, J., Zheng, B., Zhou, D.R., Qi, X. M., Tang, R., Wang, J. P., Ren, C. H., Nie, W., Chi, X. G., Xu, Z., Chen, L. D., Li, Y. Y., Che, F., Pang, N. N., Wang, H. K., Tong, D., Qin, W., Cheng, W., Liu, W. J., Fu, Q. Y., Liu, B. X., Chai, F. H., Davis, S. J., Zhang, Q., and He, K. B.: Enhanced secondary pollution offset reduction of primary emissions during COVID-19 lockdown in China, Natl. Sci. Rev., 8, 137. https://doi.org/10.1093/nsr/nwaa137, 2021.

Ianniello, A., Spataro, F., Esposito, G., Allegrini, I ., Rantica, E ., Ancora, MP., Hu, M., and Zhu, T.: Occurrence of gas phase ammonia in the area of Beijing (China), Atmos. Chem. Phys., 10, 9487-9503, https://doi.org/10.5194/acp-10-9487-2010, 2010.

Liu, M. X., Huang, X., Song, Y., Tang, J., Cao, J. J ., Zhang, X. Y., Zhang, Q., Wang, S. X., Xu, T. T., Kang, L., Cai, X. H., Zhang, H. S., Yang, F. M., Wang, H. B., Yu, J. Z., Lau, A. K. H., He, L. Y., Huang, X. F., Duan, L., Ding, A. J., Xue, L. K., Gao, J., Liu, B., and Zhu, T.: Ammonia emission control in China would mitigate haze pollution and nitrogen deposition, but worsen acid rain, Proc. Natl. Acad. Sci. U. S. A., 116, 7760-7765, https:// 10.1073/pnas.1814880116, 2019.

Pan, Y.P., Wang, Y.S., Tang, G.Q., and Wu, D.: Wet and dry deposition of atmospheric nitrogen at ten sites in Northern China, Atmos. Chem. Phys., 12(14). https://doi.org/10.5194/acp-12-6515-2012, 2012.

Sun, Y. L., Zhuang, G. S., Tang, A. H., Wang, Y., and An, Z. S.: Chemical characteristics of $PM_{2.5}$ and PM_{10} in haze-fog episodes in Beijing, Environ. Sci. Technol., 40, 3148-3155, https://doi.org/10.1021/es051533g, 2006.

Tao, J., Zhang, L.M., Ho, K.F., Zhang, R.J., Lin, Z.J., Zhang, Z.S., Lin, M., Cao, J.J., Liu, S.X., and Wang, G.H.: Impact of $PM_{2.5}$ chemical compositions on aerosol light scattering in Guangzhou—the largest megacity in South China, Atmos. Res., 135-136. https: //doi.org/10.1016/j.atmosres.2013.08.015, 2014.

Van Damme, M. Clarisse, L., Whitburn, S ., Hadji-Lazaro, J., Hurtmans, D., Clerbaux, C., and Coheur, P. F.: Industrial and agricultural ammonia point sources exposed. Nature, 564, 99. https: //doi.org/10.1038/s41586-018-0747-1, 2018.

Van Damme, M., Van Damme, M., Clarisse, L., Bauduin, S., Heald, CL ., Hadji-Lazaro, J., Hurtmans, D., Zondlo, M.A., Clerbaux, C., and Coheur, P. F.: Version 2 of the IASI NH_3 neural network retrieval algorithm: near-real-time and reanalysed datasets. Atmos. Meas. Tech. 10, 4905-4914. https: //doi.org/10.5194/amt-10-4905-2017, 2017.

Whitburn, S. Van, Damme, M., Clarisse, L., Bauduin, S., Heald, C. L., Hadji-Lazaro, J., Hurtmans, D., Zondlo, M. A., Clerbaux, C ., and Coheur, P. F.: A flexible and robust neural network IASI-NH_3 retrieval algorithm. J. Geophys. Res.-Atmos., 121, 6581-6599, https: //doi.org/10.1002/2016JD024828, 2016.

Xing, J., Liu, X., Wang, S. X., Wang, T., Ding, D., Yu, S., Shindell, D., Ou, Y., Morawska, L., Li, S. W., Ren, L., Zhang, Y. Q., Loughlin, D., Zheng, H. T., Zhao, B., Liu, S. C., Smith, K. R., and Hao, J. M.: The quest for improved air quality may push China to continue its CO_2 reduction beyond the Paris Commitment. Proc. Natl. Acad. Sci. U. S. A., 117, 29535-29542. https: //doi.org/10.1073/pnas.2013297117, 2021.

Xu, W., Song, W., Zhang, Y. Y., Liu, X. J., Zhang, L., Zhao, Y. H ., Liu, D. Y ., Tang, A. H., Yang, D. W., Wang, D. D., Wen, Z., Pan, Y. P., Fowler, D., Collett, J. L., Erisman, J. W., Goulding, K., Li, Y., and Zhang, F. S.: Air quality improvement in a megacity:

implications from 2015 Beijing Parade Blue pollution control actions, Atmos. Chem. Phys., 17, 31-46. https: //doi.org/10.5194/acp-17-31-2017, 2017.

Zhang, L., Jacob, D. J., Knipping, E. M., Kumar, N., Munger, J. W., Carouge, C. C., van Donkelaar, A., Wang, Y. X., and Chen, D: Nitrogen deposition to the United States: distribution, sources, and processes, Atmos. Chem. Phys., 12, 4539–4554, https: //doi.org/10.5194/acp-12-4539-2012, 2012.